Energy and spectral analysis of confined solar flares from radio and X-ray observations

Cheng-Ming Tan[1,2], Karl Ludwig Klein[3], Yi-Hua Yan[1,2], Satoshi Masuda[4], Bao-Lin Tan[1,2], Jing Huang[1,2] and Guo-Wu Yuan[5]

[1] CAS Key Laboratory of Solar Activity, National Astronomical Observatories of Chinese Academy of Sciences, Beijing 100101, China; *tanchm@nao.cas.cn*

[2] School of Astronomy and Space Sciences, University of Chinese Academy of Sciences, Beijing 100049, China

[3] Observatoire de Paris, LESIA & Station de radioastronomie de Nançay, Univ. PSL, CNRS, Sorbonne Univ., Univ. de Paris, Univ. d'Orléans, 5 place Jules Janssen, F- 92190 Meudon, France

[4] Institute for Space-Earth Environmental Research, Nagoya University, Nagoya 464-8601, Japan

[5] School of Information Science and Engineering, Yunnan University, Kunming 650091, China

Abstract The energy and spectral shape of radio bursts may help us understand the generation mechanism of solar eruptions, including solar flares, coronal mass ejections, eruptive filaments, and various scales of jets. The different kinds of flares may have different characteristics of energy and spectral distribution. In this work, we selected 10 mostly confined flare events during October 2014 to investigate their overall spectral behaviour and the energy emitted in microwaves by using radio observations from microwaves to interplanetary radio waves, and X-ray observations of *GOES*, RHESSI, and Fermi/GBM. We found that: all the confined flare events were associated with a microwave continuum burst extending to frequencies of $9.4 \sim 15.4\,\mathrm{GHz}$, and the peak frequencies of all confined flare events are higher than 4.995 GHz and lower than or equal to 17 GHz. The median value is around 9 GHz. The microwave burst energy (or fluence) and the peak frequency are found to provide useful criteria to estimate the power of solar flares. The observations imply that the magnetic field in confined flares tends to be stronger than that in 412 flares studied by Nita et al. (2004). All 10 events studied did not produce detectable hard X-rays with energies above $\sim 300\,\mathrm{keV}$ indicating the lack of efficient acceleration of electrons to high energies in the confined flares.

Key words: Sun: solar flare — Sun: radio burst — Sun: energy — Sun: spectral

1 INTRODUCTION

Solar flares are believed to be the most powerful explosions in the solar system. They may produce strong impact on the space weather around the Earth. However, the flares are characterized by diversity and complexity. For example, the energy released in a flare may range from above 10^{26} J in a super flare ($>$X10 flare) to less than 10^{21} J in an A-class small flare. As for their timescale, the duration may range from a few seconds to above 2 hours. So far, there is nearly a consensus that the flare energy is released through magnetic reconnection in the magnetized plasmas of the solar corona. The possible mechanism that trigger magnetic reconnection and the flare include the emerging magnetic flux model (Heyvaerts et al.

1977), the standard flare model (Shibata et al. 1995), the tether-cutting model (Moore et al. 2001, the circular ribbon flare model (Wang & Liu 2012), and the magnetic-gradient driven model (Tan et al. 2020), etc. Many flares are accompanied with very spectacular coronal mass ejections (CMEs). They are usually called eruptive flares, while at the same time there are also many flares without accompanying CMEs, which are called confined flares (Ji et al. 2003).

With such strong diversity of solar flares, it is necessary to investigate the characteristics in different flare populations, such as in different class flares, flares in different phases of solar cycles (valley, ascend, peak and descend phases of solar cycles, defined as Tan 2019), long-

Table 1 The Main Information of *GOES* Soft X-ray and Radio Emission of the Selected Events

ID	Class	Date	Start	Max.	End	IP burst	SBRS observation			NORP, RSTN	Peak freq.
							1.1–2.1 GHz	2.6–3.8 GHz	5.2–7.6 GHz	burst GHz	GHz
(1)	(2)	(3)	(4)	(5)	(6)	(7)	(8)	(9)	(10)	(11)	(12)
MF1*	M1.6	Oct18	0702	0758	0849	no	dm.FS	cont.	cont.	0.245–15.4	4.995
MF8*	M8.7	Oct22	0116	0159	0228	no	dm.FS,and cont.	cont.	cont.	0.245–35.0	9.4
MF9	M2.7	Oct22	0511	0517	0521	no	no	no	cont.	4.995–35.0	17.0
MF11*	M4.0	Oct24	0737	0748	0753	type III	dm.FS,and cont.	cont.	cont.	0.245–15.4	8.8
MF16	M7.1	Oct27	0006	0034	0044	no	no	no	cont.	4.995–35.0	17.0
MF17	M1.0	Oct27	0144	0202	0211	no	no	no	cont.	4.995–17.0	17.0
MF18*	M1.3	Oct27	0335	0341	0348	no	no	cm.FS	cont.	2.84–35.0	9.4
MF21*	M3.4	Oct28	0215	0242	0308	no	dm.FS	no data	cont.	2.0–35.0	17.0
MF22	M6.6	Oct28	0323	0332	0341	no	bad data	bad data	bad data	9.4–35.0	17.0
MF24	M1.0	Oct29	0603	0820	0852	no	no	weak cont.	cont.	2.695–15.4	15.4

Column (1) is the event ID of *GOES* SXR M-class flare, same as Chen et al. (2015). The star * marks the event with dm. or cm. fine structure. Col. (2) is the flare class. Col. (3) is the event date. Clos. (4)–(6) are the begin, peak, and end time of the SXR flare. Col. (7) indicates the interplanetary (IP) burst at decametre-hectometre wavelengths (DH). Clos. (8)–(10) indicate the fine structure bursts or continuum bursts observed by SBRS/Huairou at three bands, respectively. Col. (11) indicates the burst at the fixed frequency observed by NORP or RSTN. The last column lists the peak flux frequency that analyzed from NoRP or RSTN observations. The dm.FS or cm.FS indicates the spectral fine structure at decimeter or centimeter wavelength. The cont. indicates the continuum enhancement.

duration flares or short-duration flares, eruptive flares or confined flares, etc.

One of the main characteristics of solar flares is their energy and spectral distribution which may help us to understand the generation mechanism of solar eruptions, including solar flares, CMEs, eruptive filaments, and various scales of jets (Aschwanden et al. 1998), and to obtain the evolution of solar activity. Many people investigated the microwave spectrum of solar flares and its correlation with hard X-rays, soft X-rays, optical, radio wavelengths, and energetic particles in interplanetary space (Guidice & Castelli 1975; Aschwanden et al. 1998; Isliker & Benz 2001; Trottet et al. 2015, etc.). Nita et al. (2002, 2004) investigated the peak flux distribution of solar radio burst data observed during 1960–1999 as a function of frequency and time over a wide frequency range, and found that the distributions are well fitted by power laws over a wide range of flux densities, but diverge from a power law at both high and low flux densities. They also found that the divergence of the distribution from the fit at low flux density is probably due to sensitivity limits of the recording instruments which ranges from about 10 sfu during solar minimum to about 20 sfu during solar maximum. Fürst (1971) and Melnikov et al. (2008) studied the changes in spectral peak frequency of microwave bursts with time and found that, for the majority of simple microwave bursts, the peak frequency shows a high positive correlation with flux density, which is in qualitative agreement with theoretical expectations based on gyrosynchrotron self-absorption. Krucker et al. (2020) found that there is a highly significant correlation between the microwave (17 GHz and 34 GHz) peak flux and the nonthermal hard X-ray bremsstrahlung peak emission seen above 50 keV. However, the existing published studies do not distinguish different types of flares, and we believe

that different kinds of flares may have different energy and spectral characteristics.

In the present paper we focus on confined flare events to study their energy and spectral distributions, including the radio peak flux, the fluence or energy emitted at microwave frequencies and in soft and hard X-rays, as well as the relationships among them. A series of confined flares from one active region in October 2014 is a particularly appropriate opportunity to study flares and electron acceleration under conditions where the ambient magnetic field does not change fundamentally between individual events, and to search for correlations between different manifestations of energy release. Section 2 introduces the related observational data and definitions and extractions of parameters. Section 3 presents the main statistical results. The conclusions and the related discussions are summarized in Section 4.

2 EVENT SURVEY AND DATA ANALYSIS

In this work, we select 10 confined flares to investigate their spectral evolution from microwave to interplanetary radio wavelengths, and X-ray observations of *GOES*, Fermi/GBM, and RHESSI. Theses events occurred in solar active region AR12192 during October 2014. They were investigated by Chen et al. (2015) using the observations from the Atmospheric Imaging Assembly (AIA) and Helioseismic and Magnetic Imager (HMI) on board the Solar Dynamics Observatory (SDO).

The data used includes the radio and X-ray observations. Fixed frequency observations are provided by Nobeyama Radio Polarimeters (NoRP; Nakajima et al. 1985) at 1.0, 2.0, 3.75, 9.4, 17, and 35 GHz, and by the Radio Solar Telescope Network (RSTN) at 0.245, 0.41, 0.61, 1.415, 2.695, 4.995, 8.80, and 15.4 GHz. The RSTN monitors eight fixed frequencies at four

observatories over the world. They are located at Sagamore Hill (Massachusetts, U.S.A.), Palehua (Hawaii, U.S.A.), Learmonth (Australia), and San Vito (Italy). The spectral observations included the Chinese Solar Broadband Radio Spectrometer at Huairou (SBRS/Huairou: Fu et al. 1995, 2004) at 1.1–7.6 GHz, Mingantu Spectral Radioheliograph (MUSER: Yan et al. 2016, 2021) at 2–15 GHz, decimetric and metric spectrometers of the Yunnan Astronomical Observatories (YNAO: Gao et al. 2014) at 70–700 MHz, the Nançay Decameter Array (NDA, Lecacheux 2000) located at Nançay, France at 20–70 MHz, the ORFEES spectrograph (located at Nancay, France) at 144–1000 MHz, the Culgoora spectrograph (Australia) at 18–1800 MHz, and the Wind/WAVES radio spectrograph (Bougeret et al. 1995) at 20 kHz–13.825 MHz. The X-ray observation includes the soft X-ray (SXR) flux at 1–8Å and 0.5–4Å observed by *GOES* (Bornmann et al. 1996), hard X-ray (HXR) flux observed by the Fermi Gamma-ray Burst Monitor (Fermi/GBM, Meegan et al. 2009) and RHESSI (Lin et al. 2002).

Table 1 lists the main information of *GOES* SXR and radio emission of the selected ten events. Columns 4–6 are the start, peak, and end time of the SXR flare. Column 7 indicates whether an interplanetary type III burst was observed. Columns 8–10 give a brief characterization of different frequency ranges as to the presence of decimeter (abbreviation as dm.) or centimeter (abbreviation as cm.) fine structure (abbreviation as FS), and microwave continuum (abbreviation as cont.). Section 3 will illustrate in detail the relationship between the spectral characteristics and the flux density spectrum. Columns 11 and 12 indicate the range and peak frequency of the fixed-frequency observations. Nine events were associated with microwave continuum burst at frequencies greater than 5 GHz, the MF22 event was associated with a microwave continuum burst at frequency of greater than 9.4 GHz. The peak frequencies of all events are above 4.995 GHz.

Figure 1 presents the dynamic spectra of the ten confined flare events, as observed by Wind/Waves, Culgoora, NDA, Ynao, ORFEES, and SBRS/Huairou. Five events are accompanied by groups of dm. or cm. fine structure, which are presented in Figure 2.

Panel (1) of Figure 1 presents the observed spectrum on 2014 Oct. 18 (event MF1, 07:02–08:49 UT). The start and end time of MF1 are marked by white lines. The green curves are flux profiles at single frequencies of 1356 MHz, 2840 MHz, and 5900 MHz, respectively. The event shows no spectral fine structure on the microwave continuum burst in the frequency range of 2.6–3.8 GHz and 5.2–7.6 GHz. There are spectral fine structures on the continuum burst of 1.1–2.1 GHz. Panel (1) of Figure 2

presents the details of the fine structures. They are groups of type III bursts with fast frequency drift rates. At lower frequencies the Culgoora and Wind/Waves radio spectra (20 kHz∼100 MHz) showed no counterpart of event MF1.

Panel (2) of Figure 1 presents the observed spectrum on 2014 Oct. 22 (events MF8, 01:16–02:28 UT, and MF9, during 05:11–05:21UT) observed by Wind/Waves, Ynao, and SBRS/Huairou. There are continuum bursts in the frequency range of 2.6–3.8 GHz and 5.2–7.6 GHz around the MF8 event, without spectral fine structure. Groups of type III bursts with fast downward and upward drifts are seen on top of the continuum in the frequency range 1.1–2.1 GHz. Panel (2) of Figure 2 presents the details of this fine structure. The Ynao radio spectrum showed no counterpart to this event. The Wind/Waves spectrum showed an IP type III burst about 30 minutes afterwards, which had no connection with the main microwave burst. Around the MF9 event, there is only an impulsive burst in the frequency of 5.2–7.6 GHz observed by SBRS/Huairou and in the frequency range $4.0 \sim 15$ GHz observed by MUSER without spectral fine structure. This is presented in panel (3) of Figure 2.

Panel (3) of Figure 1 presents the observed spectrum on 2014 Oct. 24 (event MF11, 07:37–07:53UT) observed by Wind/Waves, Culgoora, Ynao, ORFEES, and SBRS/Huairou. All bands of SBRS/Huairou observed the continuum burst. There are spectral QPP structures in the frequency range of 1.1–2.1 GHz, which are presented in panel (4) of Figure 2. At low frequencies, the Ynao, Culgoora radio, and Wind/Wave spectrum at 25–700 MHz showed a typical type III burst. The presence of type III emission at meter-to-kilometer wavelengths is an exceptional finding in confined flares in general (Gopalswamy et al. 2009; Klein et al. 2010), and in the flares from the October 2014 active region in particular. Chen et al. (2015) reported that this event originated from the periphery of the active region, and was accompanied by a jet. We concluded that it is because of this exceptional location that the electrons had access to open field lines extending to the high corona and into the interplanetary space.

Panel (4) of Figure 1 presents the observed spectrum on 2014 Oct. 27 (event MF16, 00:06–00:44 UT, MF17, 01:44–02:11UT, and MF18, 03:35–03:48UT) observed by Wind/Waves, Culgoora, Ynao, and SBRS/Huairou. During these three events, there are continuum bursts in the frequency of 5.2–7.6 GHz, while no continuum burst is observed in the ranges 2.6–3.8 GHz and 1.1–2.1 GHz. Around the MF18 event in the frequency of 2.6–3.8 GHz, there is a small group of very weak ($S_{\text{burst}} \approx S_{\text{bg}} + 3\sigma$) and very short duration (< 1 second) of drifting burst,
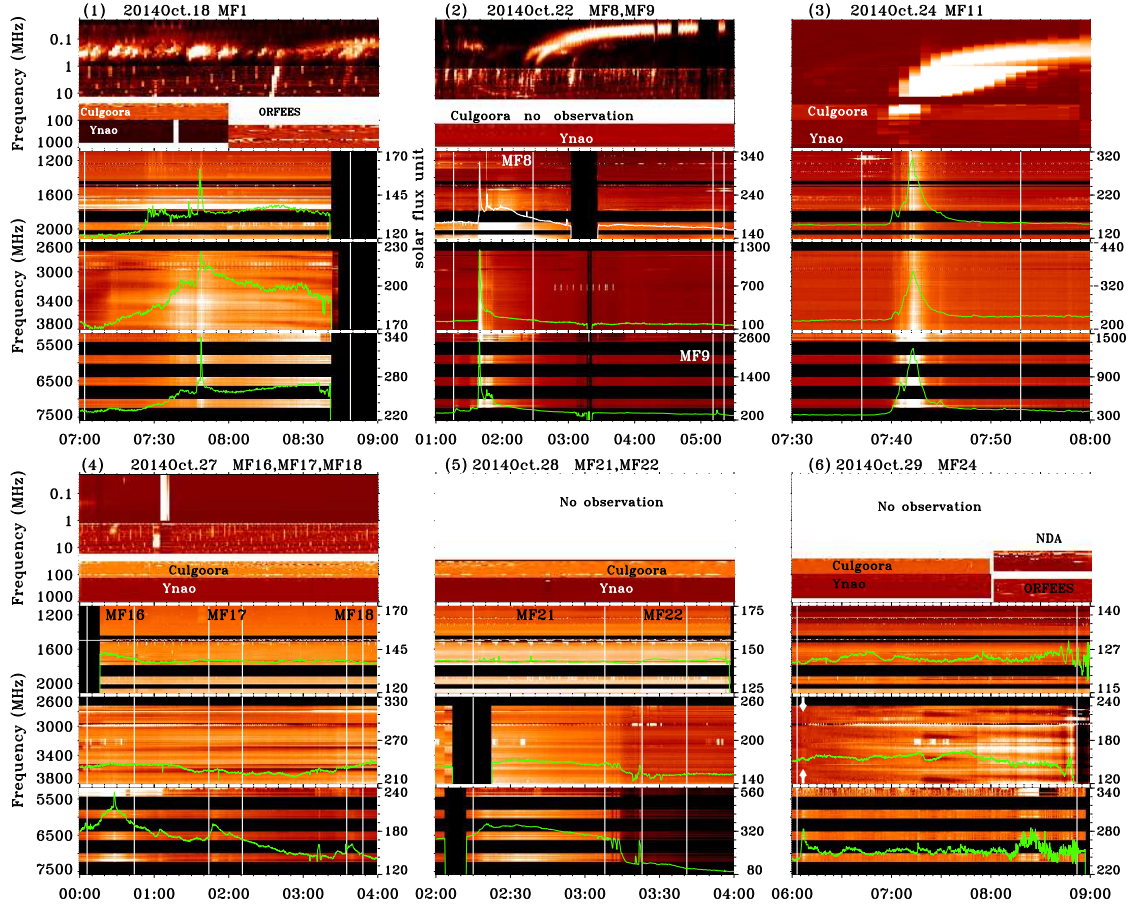
Fig. 1 Radio spectra of ten flare events on six days of October 2014. Each panel presents a daily spectrum obtained from Wind/Waves, Culgoora, NDA, Ynao, ORFEES, and SBRS/Huairou. The *white lines* mark the begin and end time of the event. The *green curves* are the flux profiles at 1356 MHz, 2840 MHz, and 5900 MHz, respectively. The tick values at the right side of the panel indicate the flux density in solar flux units. The 5.2–7.6 GHz band is only partially observed.

which is presented in panel (5) of Figure 2. Below 1.0 GHz there is no counterpart of any of these events.

Panel (5) of Figure 1 presents the observed spectrum on 2014 Oct. 28 (events MF21, 02:15–03:08UT, and MF22, 03:23–03:41UT) observed by Culgoora, Ynao, and SBRS/Huairou. For the MF21 event, a continuum burst is observed in the frequency range of 5.2–7.6 GHz and several groups of narrowband weak fine structures with fast drifts in the frequency range of 1.1–2.1 GHz. They are presented in panel (6) of Figure 2. For the MF22 event, there is no radio burst at any band below 7.6 GHz. Panel (5) of Figure 3 shows only radio emission at frequencies above 9.4 GHz.

Panel (6) of Figure 1 presents the observed spectrum on 2014 Oct. 29 (event MF24, 06:03–08:52UT) observed by Culgoora, Ynao, ORFEES and SBRS/Huairou. There are continuum bursts at the beginning (06:05UT) and peak time (08:20UT) of the event, in the frequency range of 5.2–7.6 GHz. There is only a very weak continuum

burst (indicated by two white arrows) at the beginning (06:05UT) of the event in the frequency of 2.6–3.8 GHz.

Figure 3 presents the composed figure of *GOES* SXR flux and radio flux of the ten confined flare events. For each day's panel, the top mini panel shows the profiles of *GOES* SXR flux at 1–8Å (red curve) and 0.5–4Å (blue curve). The start-end time and peak time are marked as the vertical blue line and red line, respectively. In the bottom mini panels the radio flux is plotted at eight frequencies (245, 410, 610, 1415, 2695, 4995, 8800, and 15400 MHz) observed by Palehua (Hawaii) of RSTN or at six frequencies (1000, 2000, 3750, 9375, 17000 and 35000 MHz) observed by NORP. The start-end time (blue line) are the same as SXR event time. The peak time (red line) are calculated as maximum time of microwave burst considering most frequencies. For the long duration event with multiple peak time, for example the event of 2014 Oct. 29, only the closest one to the SXR peak time was selected. The peak time of radio flux are about 1∼20 minutes earlier than that of SXR. This is consistent with
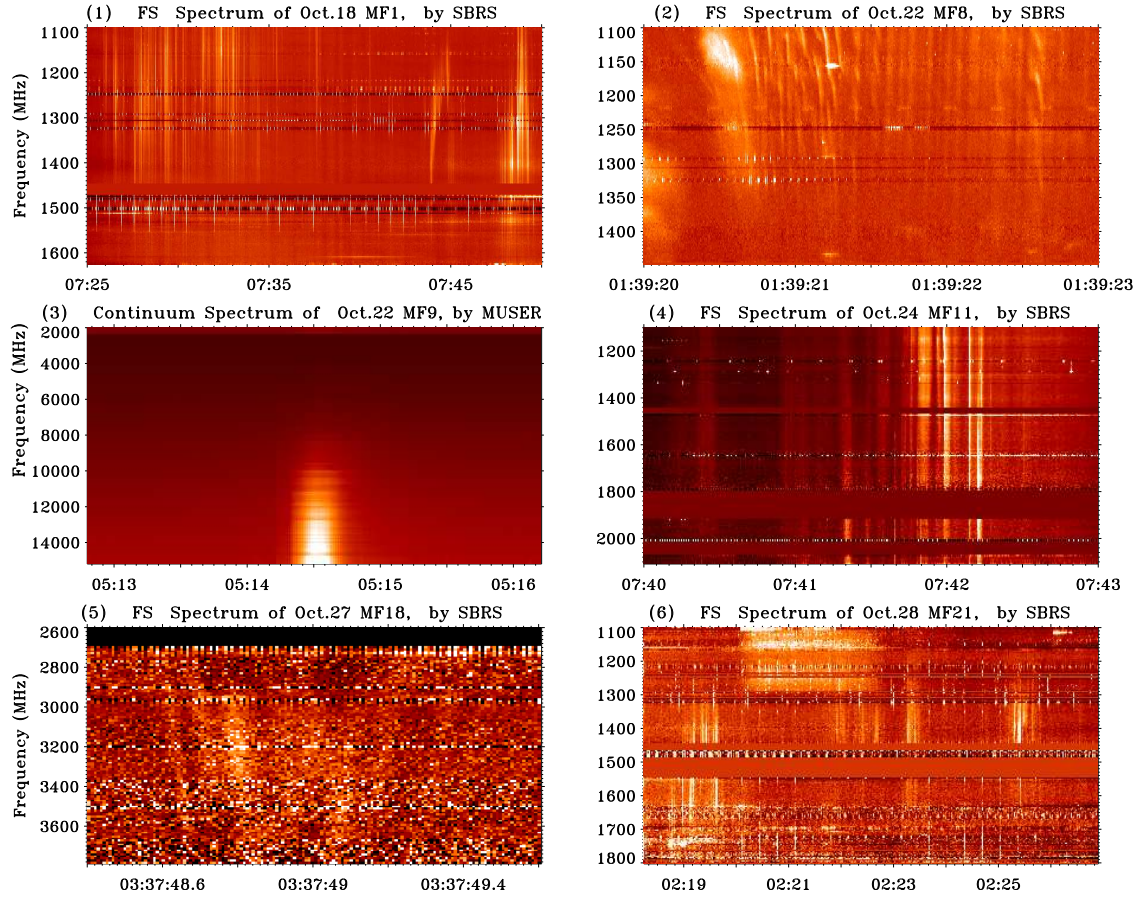
Fig. 2 The spectrum of fine structures (abbreviation as FS) in five events observed by SBRS and one impulsive microwave continuum burst observed by MUSER.

the result of Krucker et al. (2020). Figure 3 also shows that the rapid increase of SXR light curve is very close to the maximum of HXR flux (orange line) or the microwave light curves. This is consistent with the deduction of the Neupert effect (Neupert 1968; Ning & Cao 2010). The green areas designated the integrated radio flux in events and at frequencies where the burst was clearly identified. In the panel of 2014 Oct. 18, the integrated radio flux (green area) of the MF1 event at 245, 410, and 610 MHz was not plotted because of strong radio interference. In the panel of 2014 Oct. 27, the time range (blue line) of the third event (MF18) did not include the radio burst just before the event. But the flux value of this event is still kept for the later energy analysis. In the panel of 2014 Oct. 28, the mini panel of radio observations shows the flux profile had some jumps (gray line) around the burst. The jumps were corrected as shown by the black lines. The MF22 event showed the radio burst happened only above 9.4 GHz. In the panel of 2014 Oct. 29, the MF24 is a long duration event with multiple flares. The radio flux of the background decreased or increased along the time because of some uncertain reason. A time-varying background had

to be subtracted to calculate the flux of the burst. The calculation of background and subtraction were indicated in the quantitative analysis part after.

The Fermi or RHESSI HXR counts flux profiles of the ten confined flare events are shown in Figure 4. Some events are with good Fermi observation, while some events are not. Only the better one was included. Most of the events have no credible flux enhancement above ~ 50 keV. All the events has no credible flux enhancement at energy of higher than 300 keV. For each event, the right panel shows the photons flux spectra of the event. Both the counts flux and photons flux spectrum were analyzed with solar software (SSW). The SSW supplied sets of program and tools. Thus the counts flux and photons flux can be obtained. The integrated photon flux (fluence) spectrum is the integration of all the photon flux within the event time (red lines in Fig. 4).

In the following we conduct a quantitative analysis in order to search for correlations. For microwave bursts we consider the peak flux density, the flux density integrated over the entire event at a given frequency (fluence), and
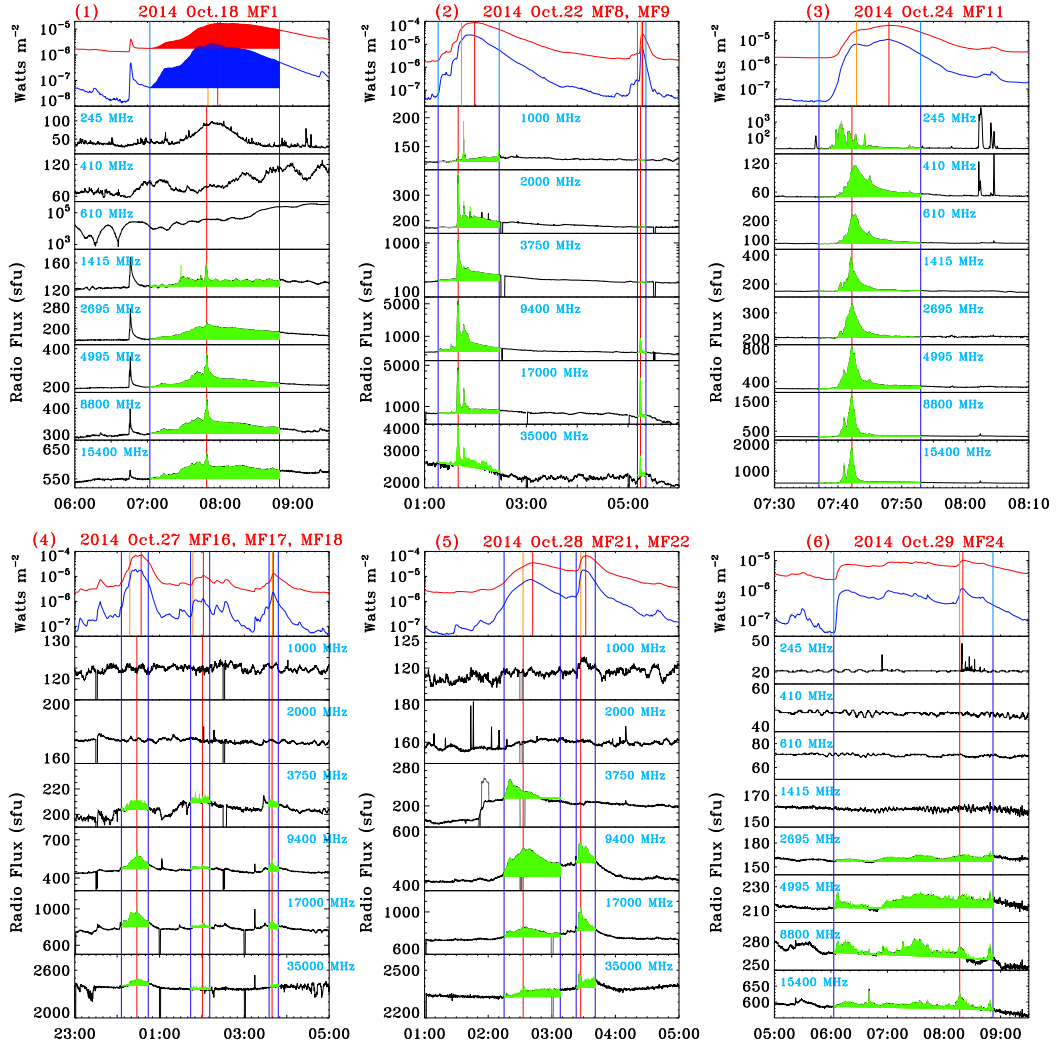
Fig. 3 Composed figure of *GOES* SXR flux and radio flux of ten events during six days. For each day, the *GOES*-15 soft X-ray flux is plotted in the top mini panel, and the radio flux of RSTN or NORP observation at several frequencies in the bottom mini panels. As an example, top of panel (1), the integrated SXR flux of the flare after background subtraction is displayed by *red* (1–8Å) and *blue* (0.5–4Å) *shading*. The *vertical blue* and *red lines* mark the start-end time and the peak time, respectively. The *vertical orange line* is the HXR peak time. The *green area* is the integrated radio flux of the burst after background subtraction.

the total energy radiated during the microwave burst. For reference we consider the SXR peak flux and fluence.

(1) Background radio flux ($S_{bg}(\nu)$): The background flux density, which must be subtracted, was calculated as the average value during a time interval lasting several minutes outside the *GOES* SXR event, avoiding any period of enhanced solar radio emission or terrestrial interference. The standard deviation was also calculated during this interval, and the time of the burst was considered as the time interval where the flux density exceeds the background plus three times the standard deviation. The solar flux unit is 1sfu=10^{-26} J s^{-1} m^{-2} Hz^{-1}.

(2) Peak radio flux ($S_{peak}(\nu)$): This is the peak flux value during the event (vertical red line in Fig. 3), after

subtraction of the pre-event background. In the microwave band > 1 GHz, the peak times are almost the same at different frequencies in most cases.

(3) Radio fluence at a single frequency ($Fluen(\nu)$): This is the integral of the radio flux density during the burst after background-subtraction (the green area in Fig. 3) at a single frequency ν. For some events the $Fluen(\nu)$ at low frequencies were not plotted because of interference. Practically $Fluen(\nu)$ is calculated as the sum

$$Fluen(\nu) = \sum_{i=m}^{n} (\frac{1}{2}[S_{i+1} + S_i - 2 \times S_{bg}] \times [t_{i+1} - t_i]).$$

(1)

Here, S_i is the instantaneous radio flux of the burst, ν is frequency, $i = m \rightarrow n$ is the data number, t is the time in
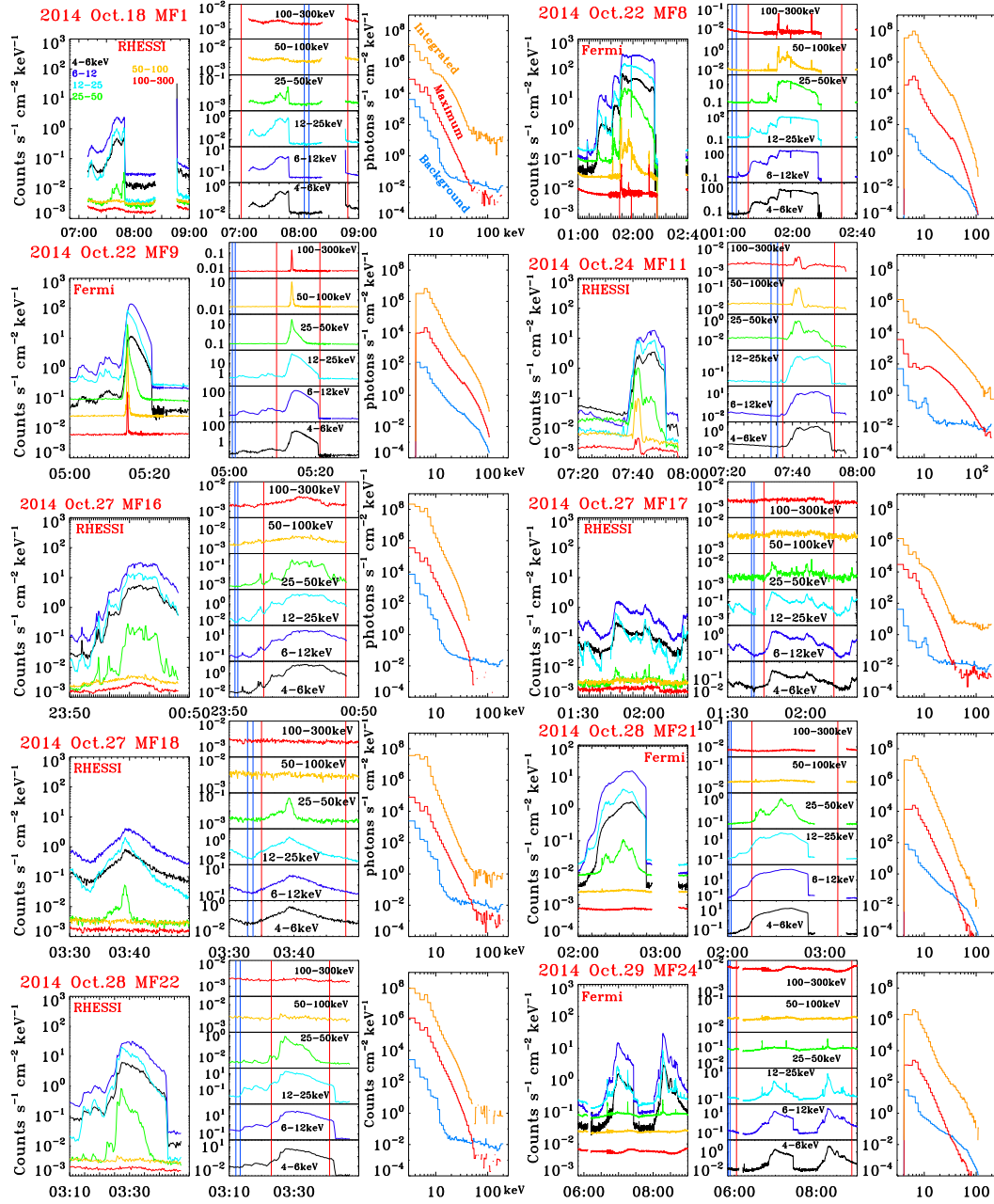
Fig. 4 Fermi or RHESSI HXR counts flux and photons flux spectra of ten events. For each event, the HXR flux of six energy bands is plotted in the left mini panel by different colors. The *vertical red* and *blue lines* mark the event time and the background intervals, respectively. In the panel of the photons flux spectrum the *blue lines* show the flux spectra of the background. The *red lines* show the peak flux spectra after background subtraction. The *orange lines* are the integrated photons flux (fluence) spectra after background subtraction.

seconds. Equation (1) gives the fluence of the radio burst in units of J m^{-2} Hz^{-1}.

(4) Radio burst total energy (E_{total}): The total energy of the radio burst can be calculated by summing the fluences over frequency, as in Equation (2), using only interference-free frequencies above 1 GHz. The unit is

J m^{-2}.

$$E_{\text{total}} = \sum_{i=m}^{n} (\frac{1}{2}[Fluen(\nu_{i+1}) + Fluen(\nu_i)] \times [\nu_{i+1} - \nu_i]).$$

(2)

(5) Background SXR flux ($F_{\text{SXR\_bg}}$): It was calculated as the average value of several minutes before the *GOES* SXR event time (vertical blue line in Fig. 3). The SXR flux unit is Watt m^{-2}.
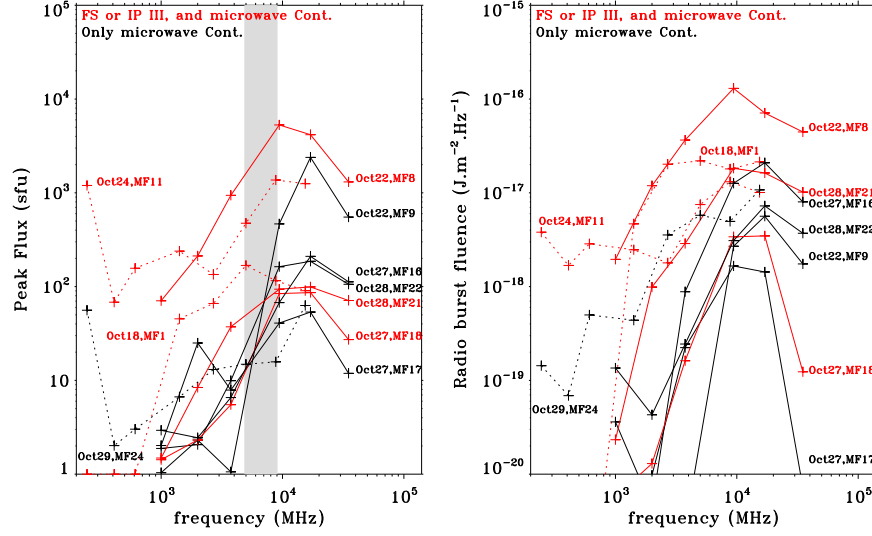
Fig. 5 The flux and fluence spectral characteristics of the confined flares. The left panel presents the peak flux spectrum. The *grey shading* is the median range (4.9 ∼ 9 GHz) of peak frequency reported by Nita et al. (2004). The right panel plots the radio burst fluence versus frequencies. The flux value is calculated after subtracting the background radio flux.
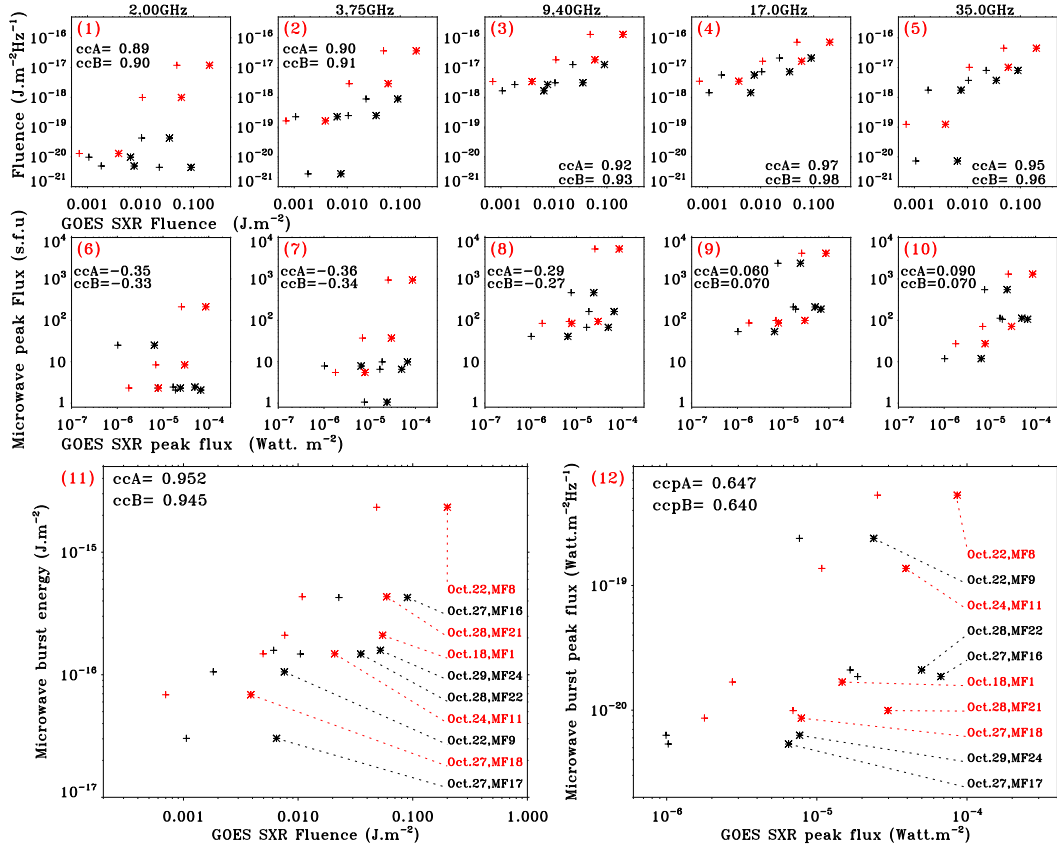

Fig. 6 Panels (1)–(5) plot the microwave burst fluence at five NORP frequencies versus SXR fluence in the two *GOES* bands. Panels (6)–(10) plot the microwave burst peak flux at five NORP frequencies versus SXR peak flux in the two *GOES* bands. Panel (11) plots the microwave burst energy versus SXR fluence in the two *GOES* bands. Panel (12) plots the microwave burst peak flux versus SXR peak flux in the two *GOES* bands. The cross and star symbols are microwave burst versus SXR flare of *GOES* 0.5–4Å (A band) and 1–8Å (B band), respectively. The correlation coefficients (ccA and ccB) between microwave burst and SXR flare in the two *GOES* bands are indicated. *Red* and *black symbols* distinguish the two event classes as in Fig. 5.
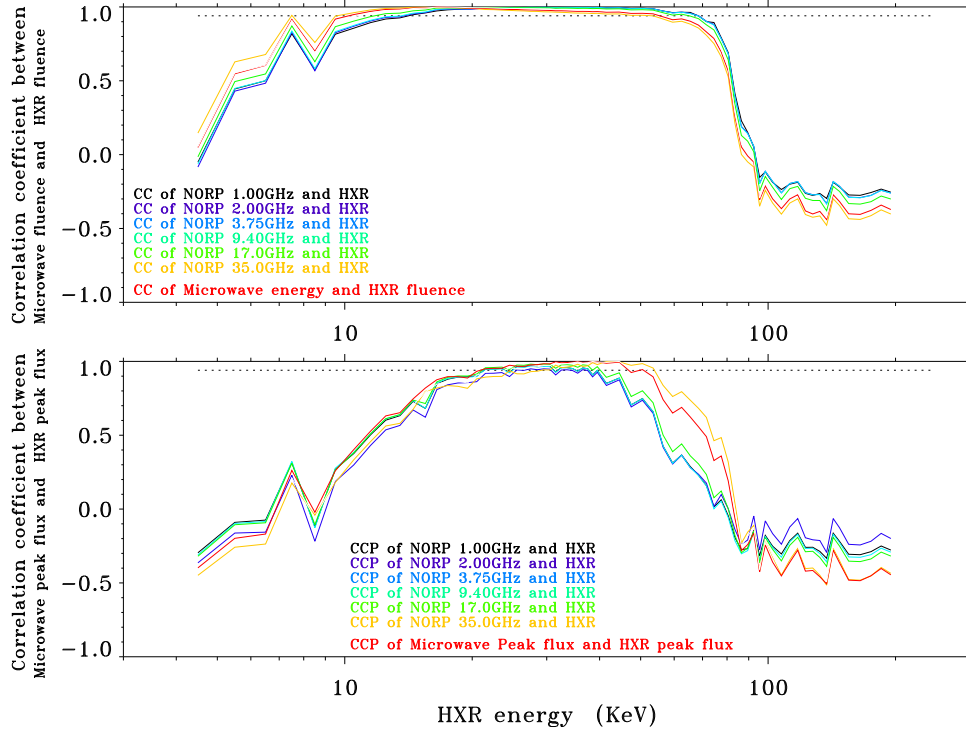
Fig. 7 The upper panel plots the correlation coefficients between microwave burst fluence at NORP six frequencies (*different color*) and HXR fluence in 76 raw bands within 4–250 keV. The *red line* is the correlation coefficients between microwave burst energy and HXR fluence. The *dashed line* marks the value of 0.94 which decided by all the cases within 15–50 keV. The bottom panel plots the peak flux correlation coefficients between microwave burst at NORP six frequencies and HXR flare in 76 raw bands within 4–250 keV. The *red line* is the correlation coefficients between microwave burst peak flux (maximum value within NORP 1–35 GHz) and HXR peak flux.

(6) Peak SXR flux ($F_{\mathrm{SXR\_peak}}$): This is the peak value during the SXR flare event. Usually it is defined as the SXR flare class .

(7) SXR fluence ($Fluen_{\mathrm{SXR}}$): It was calculated as the integral of the background-subtracted SXR flux during the flare at a single band. The unit is J m^{-2}. In the top panel (1) of Figure 3, the red area is $Fluen_{\mathrm{SXR}}$ at 1–8Å (A band) and the blue area is $Fluen_{\mathrm{SXR}}$ at 0.5–4Å (B band). It can be calculated with the analogue of Equation (1).

In the next section, we will present the statistical results of the energy, spectral characteristics and the related correlations.

3 RESULT

This section illustrates the results of our analysis. The first subsection analyzes the spectral characteristics of the ten confined flare events, the relationship between the spectral characteristics and the flux spectrum, and the relationship between the spectral characteristics and the fluence spectrum. The spectral characteristics include the microwave continuum, centimeter and decimeter spectral fine structures, and bursts at meter-kilometer wavelengths. The second subsection analyzes the relationships between

microwave burst and *GOES* SXR flare. The third subsection analyzes the relationships between microwave burst and HXR flare.

3.1 The Spectral Characteristic of the Confined Flares

According to the above analysis in Section 2, we may classify ten confined flare events into two classes. The first class events were accompanied by decimeter or centimeter spectral fine structure or IP burst (only one case), and also microwave continuum burst. The microwave spectra of this class are plotted in red color in Figure 5. The 2nd class events have only microwave continuum at frequencies higher than 2.695 GHz, without spectral fine structure or IP burst. The spectra are plotted in black color in Figure 5.

Figure 5 displays the peak flux spectra and the fluence spectra of ten confined flare events. The left panel shows the peak flux spectrum. The flux value is calculated after subtracting the background radio flux $S_{\mathrm{bg}}(\nu)$. The calculation was illustrated in Section 2 and Figure 3. In the microwave band, Table 1 and the left panel of Figure 5 show that the peak frequency of all events is greater than or equal to 4.995 GHz. The peak frequency of the events with fine structures is lower than or equal to 17 GHz. The peak

frequency of the events without fine structures is $15.4 \sim 17$ GHz. In the right panel the radio burst fluence is plotted versus frequency. The radio burst fluence of the events with fine structure tends to be higher than that of the events without fine structure. The event of 2014 Oct. 29 MF24 is an unusual long duration event with multiple energy releases, thus the radio burst fluence is slightly higher than other events without fine structure. The MF18 burst has the lowest fluence among the events with fine structure, but the fine structure itself is also faint ($S_{\mathrm{burst}} \approx S_{\mathrm{bg}} + 3\sigma$) and of very short duration (< 1 second). So this is consistent with an overall trend that events with fine structure have higher peak flux and higher fluence than events without fine structure.

3.2 The Relationships between Microwave Peak Flux, Fluence, Energy and SXR Peak Flux, Fluence

The microwave burst peak flux, fluence, energy and SXR peak flux, fluence of all ten events were calculated with the method illustrated in Section 2. Figure 6 shows the relationship between microwave burst and *GOES* SXR flare. Panel (1)–(10) plotted the relationship between NORP microwave burst and *GOES* SXR flare, only seven events with NORP observation were included, while the other three events with only RSTN observation were not because the frequencies are different. The correlation coefficients between microwave burst fluence and SXR fluence are > 0.89 in the frequency range of 2–35 GHz. While the correlation coefficients between microwave burst peak flux at single frequency and SXR peak flux are very poor or negative. The highest correlation coefficient is microwave fluence at 17 GHz and SXR fluence. Panels (11) and (12) show that the correlation coefficients between microwave burst energy and SXR fluence are much higher than the correlation coefficients between microwave burst peak flux and SXR peak flux. The correlation coefficient between the microwave burst and the SXR flare in two bands are approximative.

3.3 The Relationships between Microwave Peak Flux, Fluence, Energy and HXR Peak Flux, Fluence

The HXR photons flux and fluence were calculated with SSW. Figure 7 plotted the correlation coefficients between microwave burst fluence or peak flux at NORP six frequencies and HXR fluence or peak flux in 76 raw bands within 4–250 keV. Only seven events with NORP observation were including. From the figure we can obtain results: 1) The correlation coefficients within 15–50 keV are higher than that < 15 keV or > 50 keV. The correlation below 10 keV or up 80 keV are poor or negative. 2) Below 80 keV, the fluence correlation coefficients is slightly higher than peak flux correlation coefficients for most energy bands. 3) The peak flux or fluence correlation coefficients have no significant difference among different frequencies in the range of 1–35 GHz. However, in the HXR 40–80 keV band, there is a weak trend that peak flux correlation between microwave at 35 GHz and HXR are higher than that at low frequencies. 4) The correlation between microwave burst total energy and HXR fluence has no significant difference compared to that between microwave burst fluence at six frequencies and HXR fluence. Also, the correlation between microwave burst peak flux (maximum value within NORP 1–35 GHz) and HXR peak flux has no significant difference compared to that between microwave burst peak flux at six frequencies and HXR peak flux.

4 CONCLUSION AND DISCUSSION

From the above multi-wavelength observations and statistical analysis on the energy and spectral characteristics of the confined flares we obtained the following conclusions:

(1) All the confined flare events were associated with microwave continuum burst extending to frequencies of greater than 9.4 GHz. Five events were associated with spectral fine structures at decimeter or centimeter wavelengths. With the exception of one single event where a type III burst was observed, the radio emission of the confined flares did not extend to meter wavelengths or beyond.

(2) The peak frequencies of all confined flare events are higher than 4.995 GHz and lower than or equal to 17 GHz.

(3) The radio burst fluence in the range 2–35 GHz of the events with spectral fine structures tends to be higher than that of the events without spectral fine structure. The trend is less clear for the peak flux.

As we mentioned above, it is interesting that there is one event accompanied by an IP type III burst at meter-to-kilometer waves, while about half of the flares of class M or above are accompanied by IP type III bursts (Kou et al. 2020). Confined flares usually have no radio emission at meter wavelengths or beyond (Gopalswamy et al. 2009; Klein et al. 2010), because the energetic electrons do not get access to magnetic structures that extend high into the corona. Nine out of the ten events studied here confirm this. The event with a type III burst was exceptional in that it was located in the periphery of the active region, rather than in the core (Chen et al. 2015), i.e. at a place where energetic particles are indeed expected to get access to open magnetic field lines (Axisa 1974; Zlobec et al. 1990; Poquérusse & McIntosh 1995; Hofmann & Ruždjak 2007). The event is hence in line with the nine confined events, and confirms the picture of electron confinement

when the energy release occurs in the core of strong magnetic fields.

It is not a surprise that half of the confined flares are accompanied by spectral fine structure, given that Tan et al. (2019) reported some small or micro flares can still generate radio fine structure. The peak frequency of all confined events is between 4.995 and about $17\,\mathrm{GHz}$, and $\geq 9\,\mathrm{GHz}$ for nine of them. This is higher than the usual median range of $4.9 \sim 9\,\mathrm{GHz}$ (Nita et al. 2004). The higher peak frequency indicates stronger magnetic field in the source region, considering microwave bursts to be generated by the gyrosynchrotron mechanism (Dulk 1985). This indicates that the magnetic field surrounding the energy release region of a confined flare is stronger than that of the normal events. This result is consistent with earlier work on confined flares (Wang & Zhang 2007; Masson et al. 2017; Amari et al. 2018; Baumgartner et al. 2018; Li et al. 2019). The radio burst energy of the events with fine structure tends to be higher than that of the events without fine structure. Such a trend is more pronounced for the energy than that for the peak flux. We suggest that the occurrence probability of fine structure is more strongly related with the emitted microwave energy than with peak flux. The radio spectral fine structures are always generated by energetic electrons accelerated in the flare, and the radio spectral fine structure can be regarded as a signal of accelerated electrons in the flare event. Therefore the flare event with radio spectral fine structures may involve much more energy than that without radio spectral fine structures.

We analyzed the relationship between microwave burst and *GOES* SXR, the relationship between microwave burst and HXR, and found that:

(1) The correlation coefficients between microwave burst fluence (or total energy) and *GOES* SXR fluence are much higher than that between microwave burst peak flux and *GOES* SXR peak flux.

(2) The correlation between microwave burst and HXR shows that: 1) The correlation coefficients within HXR 15–50 keV are higher than other energy bands. 2) For most energy bands below 80 keV, the correlation coefficients between microwave burst fluence (or total energy) and HXR fluence are slightly higher than peak flux correlation coefficients. 3) In the HXR 40–80 keV band, there is a weak trend that peak flux correlation between microwave at 35 GHz and HXR are higher than that at low frequencies.

The microwave burst fluence or total energy is a much more precise estimate of the importance of an event than the peak flux. For example, the 2014 Oct.22 MF9 event is a moderate M2.7 flare with a very strong microwave burst with peak flux $>$ 2300 sfu at 17 GHz. No radio emission is observed below 4 GHz. Figure 5 and Figure 6 show that

the peak flux is high, while the fluence and total energy is low. Figure 7 shows high correlation coefficient (≥ 0.94) between microwave burst fluence (or total energy) and HXR fluence in 15–50 keV. They are slightly higher than peak flux correlation between microwave burst and HXR flare for most energy bands below 80 keV. The peak flux correlation only shows high coefficient (≥ 0.94) between microwave burst at 17–35 GHz and HXR flare in the 30–40 keV. This is a clue that with microwave burst fluence or total energy one can estimate a flare in a wide range globally, while with peak flux one can diagnose a flare partially.

In Figure 7, the correlation coefficient between microwave burst fluence (or peak flux) and HXR fluence (or peak flux) is higher in the 15–50 keV range than 4–15 keV. This is consistent with the fact that both the higher-energy HXR emission and the microwave emission are produced by nonthermal electrons. The decreased correlation coefficient in the 50–100 keV range, and the negative coefficient above 100 keV indicates the lack of HXR photons with energy above around 50 keV in the considered confined flares. Figure 4 also shows that most of the confined flares had no significant HXR photons flux increase above 50 keV, that is, the background spectrum dominates above 50 keV. While Krucker et al. (2020) demonstrated the microwave (17 GHz and 34 GHz) peak flux shows good linear correlation with the nonthermal hard X-ray bremsstrahlung peak emission above 50 keV. Our finding of a reduced efficiency of electron acceleration to very high energies extends the finding by Thalmann et al. (2015) for the X1.6 flare on Oct. 26.

In conclusion, the microwave burst energy (or fluence) and peak frequency are better than radio peak flux to estimate the power of flare. It is consistent with the result of Grechnev et al. (2015). Thus in general, the microwave burst energy (or fluence) is one of the most important parameters determining ability of solar flare events to produce high energy particles. The energies to which electrons are accelerated in confined flares tend to be lower than in eruptive flares, while the magnetic field around the energy release region is stronger. However, only ten confined flares were studied in this work, and they belong to the same active region. In future work, we will extend the analysis to more confined flares, and other populations of flare events in more active regions.

References

Amari, T., Canou, A., Aly, J.-J., et al. 2018, Nature, 554, 211

Aschwanden, M. J., Dennis, B. R., & Benz, A. O. 1998, ApJ, 497, 972

Axisa, F. 1974, Sol. Phys., 35, 207

Baumgartner, C., Thalmann, J. K., & Veronig, A. M. 2018, ApJ, 853, 105

Bornmann, P. L., Speich, D., Hirman, J., et al. 1996, in Society of Photo-Optical Instrumentation Engineers (SPIE) Conference Series, 2812, *GOES*-8 and Beyond, ed. E. R. Washwell, 291

Bougeret, J. L., Kaiser, M. L., Kellogg, P. J., et al. 1995, Space Sci. Rev., 71, 231

Chen, H., Zhang, J., Ma, S., et al. 2015, ApJL, 808, L24

Dulk, G. A. 1985, ARA&A, 23, 169

Fu, Q., Qin, Z., Ji, H., & Pei, L. 1995, Sol. Phys., 160, 97

Fu, Q., Ji, H., Qin, Z., et al. 2004, Sol. Phys., 222, 167

Fürst, E. 1971, Sol. Phys., 18, 84

Gao, G., Wang, M., Dong, L., et al. 2014, New Astron., 30, 68

Gopalswamy, N., Akiyama, S., & Yashiro, S. 2009, in Universal Heliophysical Processes, eds. N. Gopalswamy & D. F. Webb, 257, 283

Grechnev, V. V., Kiselev, V. I., Meshalkina, N. S., & Chertok, I. M. 2015, Sol. Phys., 290, 2827

Guidice, D. A., & Castelli, J. P. 1975, Sol. Phys., 44, 155

Heyvaerts, J., Priest, E. R., & Rust, D. M. 1977, ApJ, 216, 123

Hofmann, A., & Ruždjak, V. 2007, Sol. Phys., 240, 107

Isliker, H., & Benz, A. O. 2001, A&A, 375, 1040

Ji, H., Wang, H., Schmahl, E. J., et al. 2003, ApJL, 595, L135

Klein, K. L., Trottet, G., & Klassen, A. 2010, Sol. Phys., 263, 185

Krucker, S., Masuda, S., & White, S. M. 2020, ApJ, 894, 158

Kou, Y. K., Jing, Z. C., Cheng, X., et al. 2020, ApJL, 898, L24

Lecacheux, A. 2000, Washington DC American Geophysical Union Geophysical Monograph Series, 119, 321

Li, T., Liu, L., Hou, Y., & Zhang, J. 2019, ApJ, 881, 151

Lin, R. P., Dennis, B. R., Hurford, G. J., et al. 2002, Sol. Phys., 210, 3

Masson, S., Pariat, É., Valori, G., et al. 2017, A&A, 604, A76

Meegan, C., Lichti, G., Bhat, P. N., et al. 2009, ApJ, 702, 791

Melnikov, V. F., Gary, D. E., & Nita, G. M. 2008, Sol. Phys., 253, 43

Moore, R. L., Sterling, A. C., Hudson, H. S., & Lemen, J. R. 2001, ApJ, 552, 833

Nakajima, H., Sekiguchi, H., Sawa, M., et al. 1985, PASJ, 37, 163

Neupert, W. M. 1968, ApJL, 153, L59

Ning, Z., & Cao, W. 2010, ApJ, 717, 1232

Nita, G. M., Gary, D. E., Lanzerotti, L. J., & Thomson, D. J. 2002, ApJ, 570, 423

Nita, G. M., Gary, D. E., & Lee, J. 2004, ApJ, 605, 528

Poquérusse, M., & McIntosh, P. S. 1995, Sol. Phys., 159, 301

Shibata, K., Masuda, S., Shimojo, M., et al. 1995, ApJL, 451, L83

Tan, B. 2019, Advances in Space Research, 63, 617

Tan, B.-L., Yan, Y., Li, T., et al. 2020, RAA (Research in Astronomy and Astrophysics), 20, 090

Tan, C., Tan, B., Yan, Y., et al. 2019, Solar-Terrestrial Physics, 5, 3

Thalmann, J. K., Su, Y., Temmer, M., & Veronig, A. M. 2015, ApJL, 801, L23

Trottet, G., Samwel, S., Klein, K. L., et al. 2015, Sol. Phys., 290, 819

Wang, H., & Liu, C. 2012, ApJ, 760, 101

Wang, Y., & Zhang, J. 2007, ApJ, 665, 1428

Yan, Y., Chen, L., & Yu, S. 2016, in Solar and Stellar Flares and their Effects on Planets, eds. A. G. Kosovichev, S. L. Hawley, & P. Heinzel, 320, 427

Yan, Y., Chen, Z., Wang, W., et al. 2021, Frontiers in Astronomy and Space Sciences, 8, 20

Zlobec, P., Ruždjak, V., Vršnak, B., et al. 1990, Sol. Phys., 130, 31